Revealing Berry curvature of the unoccupied band in high harmonic generation

Gimin Bae ●, Youngjae Kim, and J. D. Lee[*]

Department of Physics and Chemistry, DGIST, Daegu 42988, Republic of Korea

Experimental determinations of the net Berry curvature have been made for the occupied band because they are basically available on the basis of electronic and magnetic responses of carriers occupying the band, for instance, through the measurement of the anomalous Hall effect or the magneto-optical Kerr effect. Here, we investigate the circular dichroism of the high-order harmonic generation (HHG) in undoped monolayer MoS_2. Breaking the threefold rotational symmetry of the pristine monolayer MoS_2 by applying uniaxial strain and an external bias field, we find that the third-order HHG signals deliver nonvanishing dichroic signatures. These signatures are essentially identical as the net Berry curvatures obtained from the electron-doped monolayer MoS_2 with the aforementioned symmetry broken. This finding implies an experimental challenge to observe the net Berry curvature of the unoccupied empty band, which should open another stage toward the advancement of valleytronics.

I. INTRODUCTION

Since the discovery of graphene and other two-dimensional crystalline materials, there have been numerous attempts to utilize the nontrivial geometrical property from the topological entanglement of the electronic band structures, i.e., the Berry curvature [1]. The Berry curvature enables versatile control of valley pseudospins and fundamentally determines anomalous electron motion [2–4], which should be a key concept to go beyond the silicon-based electronics. The valley magnetoelectric effect to induce a real-space valley magnetization, i.e., a real-space net Berry curvature, is observed in uniaxially strained electron-doped monolayer MoS_2 in a static electric field environment [5]. The valley magnetization is further developed to the valley magnetic domain, whose moving manipulates the anomalous transverse current feasible for device applications [6]. In the studies, the net Berry curvature is determined for the occupied band through electronic and magnetic responses of carriers occupying the band [2–6].

High harmonic spectroscopy is a powerful tool to investigate the electronic structure, optical response, and other physical properties of atoms, molecules, and condensed phases exploiting high-order harmonic generation (HHG) [7]. HHG is a nonlinear process of emitting high harmonic lights in targeted matters under an intense light field, such as molecules and solids, in particular, including topological insulators and two-dimensional materials [8–20], the frequencies of which are enumerated as n times ($n = 1, 2, 3, \cdots$) the incident light frequency ω_0. It was about a decade ago that HHG was first observed in a bulk solid of ZnO [10]. Recently, the seventh harmonic of HHG of graphene was studied in detail using terawatt-intensity elliptically polarized light [11]. Thereafter, electrically tuned HHG was demonstrated with

respect to intraband and interband dynamics in a single-wall carbon nanotube [12]. Furthermore, it has been an interesting finding that there is a change of helicity of HHG between topologically trivial and nontrivial phases on the basis of the Haldane model [13]. More recently, the dependence on the pulse frequency or the carrier-envelope phase of HHG in the topological insulator was studied [16]. Meanwhile, the magneto-HHG was examined for Fe(100) and Fe(001) [17], signals of which have been affected by spin polarization and the spin-orbit coupling (SOC). Since the valley magnetization indicates the orbital magnetic moment, it would be possible to study HHG of the valley magnetic materials just like ferromagnetic materials. In particular, under circularly polarized light, the HHG signal would depend on the light helicity so that more abundant physics could be available.

In this paper, we consider pristine (undoped) monolayer MoS_2 and calculate the nonlinear electron transports of high-order harmonics under the intense optical field employing the quantum master equation [21], which corresponds to high-order harmonic emission light, i.e., HHG. We propose the dichroic high-order harmonic generation (dHHG) as the difference in the third-order HHG spectra between the right circularly polarized (RCP) and the left circularly polarized (LCP) incident optical pulses. When applying the uniaxial strain along the armchair direction and the static electric field along the zigzag direction to the undoped monolayer MoS_2, we find the nonvanishing and substantial dHHG signals in the third-order harmonic spectra regardless of the emission direction. The dHHG spectra obtained in the two-dimensional domain of the external uniaxial strain and the bias electric field are found to be essentially the same as the net Berry curvature through the valley magnetoelectric effect (VME) in the same two-dimensional domain of the electron-doped monolayer MoS_2, which is calculated by the first-principles density functional theory. This finding delivers a message that one can observe the net Berry curvature of the unoccupied band in

_____
*jdlee@dgist.ac.kr

terms of dHHG spectroscopy without pursuing electronic and magnetic responses of carriers of the occupied band, for instance, the anomalous Hall effect or the magneto-optical Kerr effect. Furthermore, it suggests an alternative direction for exploring geometric prospects as well as electronic structures of valleytronic or topological materials, such as, in particular, two-dimensional transition metal dichalcogenides and gapped graphenes.

The paper is organized as follows. In Sec. II, we introduce the model Hamiltonian and theoretical formulation. In Sec. III, solving the quantum master equation, we provide dHHG spectra of the undoped monolayer MoS_2 with threefold rotational symmetry broken due to the external strain and the bias field and compare them with the first-principles calculations of the net Berry curvature of the electron-doped monolayer MoS_2 in the aforementioned symmetry breaking. Physical insights between them are discussed. In Sec. IV, we summarize the results and give a conclusion.

II. MODEL AND THEORETICAL FORMULATION

We consider the model Hamiltonian $H(\mathbf{k})$ for monolayer MoS_2 extended to include the spin-orbit coupling on the basis of the three-band tight-binding Hamiltonian $H^{\mathrm{TB}}(\mathbf{k})$, generally valid for group-VIB transition metal dichalcogenides, which is constructed accounting for three Mo d orbitals (d_{z^2}, d_{xy}, and $d_{x^2-y^2}$) and Mo-Mo hoppings up to the third nearest neighbors based on the symmetry of the monolayer [22,23]. In the pristine monolayer MoS_2, the nonlinear current $\mathbf{J}(\tau)$ driven by the incident optical field $\mathbf{A}(\tau)$ will be calculated by the quantum master equation [21],

$$\frac{d}{d\tau}\rho_{\mathbf{k}}(\tau) = -i[H[\mathbf{k}+\mathbf{A}(\tau)], \ \rho_{\mathbf{k}}(\tau)] + \hat{D}[\rho_{\mathbf{k}}(\tau)], \quad (1)$$

$$\mathbf{J}(\tau) = \frac{1}{(2\pi)^2} \int d\mathbf{k} \ \mathrm{Tr}[\mathbf{J_k}\rho_{\mathbf{k}}(\tau)], \quad (2)$$

where $\rho_{\mathbf{k}}(\tau)$ is the density matrix operator, $\hat{D}[\rho_{\mathbf{k}}(\tau)]$ the dephasing term, and $\mathbf{J_k}$ the current operator $-\partial H[\mathbf{k}+\mathbf{A}(\tau)]/\partial\mathbf{k}$. The Fourier transform of $\mathbf{J}(\tau)$ would then result as a sum of harmonics of the incident optical field, which would eventually emerge as the HHG spectrum $I(\omega)$, i.e., $I(\omega) \sim \omega^2|\mathbf{J}(\omega)|^2$. The Hamiltonian $H(\mathbf{k})$ to include SOC on the basis of the tight-binding Hamiltonian $H^{\mathrm{TB}}(\mathbf{k})$ (see Appendix A) is written as

$$H(\mathbf{k}) = \begin{bmatrix} H^{\mathrm{TB}}(\mathbf{k}) + \frac{\lambda}{2}L_z & 0 \\ 0 & H^{\mathrm{TB}}(\mathbf{k}) - \frac{\lambda}{2}L_z \end{bmatrix}.$$

λ is the strength of SOC and L_z (z component of the orbital angular momentum) is

$$L_z = \begin{bmatrix} 0 & 0 & 0 \\ 0 & 0 & 2i \\ 0 & -2i & 0 \end{bmatrix},$$

where the same bases as in $H^{\mathrm{TB}}(\mathbf{k})$, i.e., d_{z^2}, d_{xy}, and $d_{x^2-y^2}$, are adopted in L_z. Now the dephasing term is written as $\hat{D}[\rho_{\mathbf{k}}^{mn}(\tau)] = -\rho_{\mathbf{k}}^{mn}(\tau)(1-\delta_{mn})/T_2 - [\rho_{\mathbf{k}}^{mm}(\tau) - f_{\mathbf{k}+\mathbf{A}(\tau)}^m]\delta_{mn}/T_1$, where m and n are the band indices; T_1 and T_2 are the dephasing times

taken to be 100 and 20 fs, respectively; and $f_{\mathbf{k}}^m$ is the Fermi-Dirac distribution function of the mth band. In the calculation of HHG, we adopt the circularly polarized pulse for the incident optical field $\mathbf{A}_{\mathrm{RCP(LCP)}}(\tau)$, i.e., $\mathbf{A}_{\mathrm{RCP(LCP)}}(\tau) = (1/\omega_0)(E_0\cos\omega_0\tau\hat{\mathbf{x}} \pm E_0\sin\omega_0\tau\hat{\mathbf{y}})\cos^4(\pi\tau/T)$, where "+" and "−" mean RCP and LCP pulses, respectively. We take the pulse frequency ω_0 to be 0.26 eV, the average electric field strength E_0 to be 4.6 MV/cm, and the pulse envelope period T to be 200 fs.

Employing the quantum master equation with $H(\mathbf{k})$, one may calculate HHG for the pristine monolayer MoS_2 under the incident RCP or LCP pulse. In particular, the dichroic signal of HHG (i.e., dHHG) would be interesting because the circular dichroism is generally sensitive to the angular momentum states and, furthermore, the geometric properties of the wave function in the parameter space, for instance, the Berry curvature. We extract the dHHG signal from the difference in the HHG spectra between RCP and LCP optical pulses as shown later. In Fig. 1(a), we give a schematic of the experimental geometry for HHG of the monolayer MoS_2 under the RCP pulse possibly together with the uniaxial strain ϵ_y and the bias electric field E_{bias}. For an application of the bias electric field, its vector potential is given as follows, to avoid a sudden change,

$$\mathbf{A}_{\mathrm{bias}}(\tau) = \begin{cases} -E_{\mathrm{bias}}\left(\frac{\tau^3}{\tau_{\mathrm{bias}}^2} - \frac{0.5\tau^4}{\tau_{\mathrm{bias}}^3}\right) 0 \leqslant \tau < \tau_{\mathrm{bias}} \\ -E_{\mathrm{bias}}(\tau - 0.5\tau_{\mathrm{bias}}) \ \tau \geqslant \tau_{\mathrm{bias}} \end{cases},$$

where τ_{bias} is 50 fs and E_{bias} is 1.0×10^6 V/m. When the current due to the bias field is fully converged at $\tau \gg \tau_{\mathrm{bias}}$, the circularly polarized pulse is irradiated. Then the resulting vector potential is given by a summation of $\mathbf{A}_{\mathrm{bias}}(\tau)$ and $\mathbf{A}_{\mathrm{RCP(LCP)}}(\tau)$ in Eq. (1). The inset of Fig. 1(a) shows the valley selective HHG, which would be attributed to the conduction band entirely near the $-\mathbf{K}$ valley. In Fig. 1(b), HHG spectra for both RCP and LCP pulses are provided at $\epsilon_y = 0$ and $E_{\mathrm{bias}} = 0$, where no numerical difference results between the two HHG spectra. In addition, according to the high harmonic selection rule, in the figure, there would be found no $3m$th ($m = 1, 2, 3, \cdots$) order harmonic feature for the pristine monolayer MoS_2 with threefold rotational symmetry. Generally, for a system with n-fold rotational symmetry, $(n \times m)$-th order harmonic features are missing in HHG [8,9]. This is sharply contrasted to Fig. 1(c), where $3m$th order features are shown to be obvious since the threefold rotational symmetry is broken due to the applied uniaxial strain $\epsilon_y = 0.3\%$, although the two HHG spectra for RCP and LCP pulses at $E_{\mathrm{bias}} = 0$ are still hardly different numerically from each other.

III. RESULTS AND DISCUSSION

The dHHG signal would be extracted from the differences in HHG spectra between RCP and LCP pulses, which should be directly proportional to the net Berry curvature of the system. Under the circularly polarized pulse, the electrons would be excited to the conduction band and also accelerated by the anomalous Hall effect. In the semiclassical model, the velocity
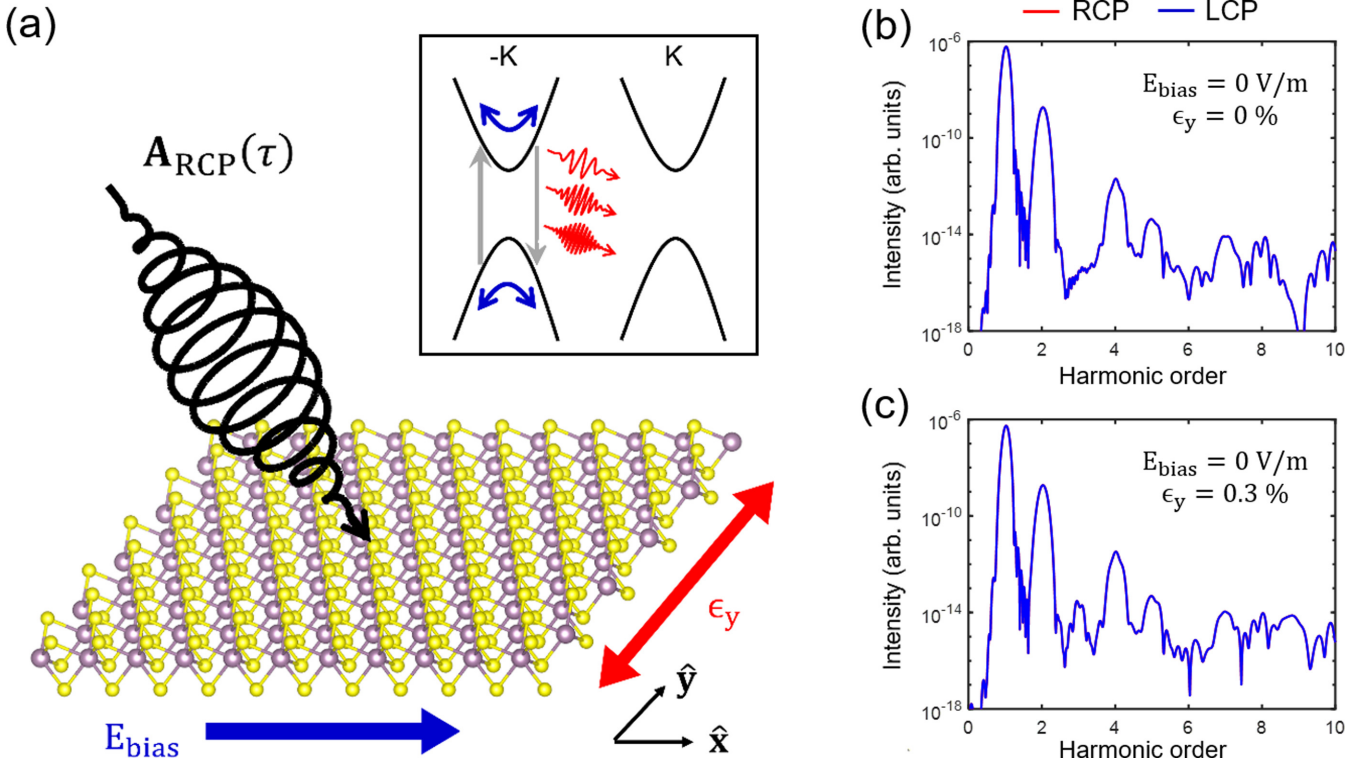
FIG. 1. Assumed geometry and calculation of HHG. (a) Geometry assumed for the HHG experiment for the monolayer MoS_2 with the tensile strain along the $\hat{\mathbf{y}}$ (armchair) direction and the bias electric field along the $\hat{\mathbf{x}}$ (zigzag) direction. Inset shows the electron or hole dynamics associating HHG under the RCP pulse pumping. (b,c) Calculation of HHG under RCP and LCP pulse pumpings (b) at $E_{bias} = 0$ V/m and $\epsilon_y = 0\%$ and (c) at $E_{bias} = 0$ V/m and $\epsilon_y = 0.3\%$.

of the electron can be written as

$$\dot{\mathbf{r}}(\tau) = \nabla_{\mathbf{k}}\varepsilon[\mathbf{k} + \mathbf{A}_{RCP(LCP)}(\tau)] + e\mathbf{E}_{RCP(LCP)}(\tau)$$
$$\times \mathbf{\Omega}[\mathbf{k} + \mathbf{A}_{RCP(LCP)}(\tau)], \qquad (3)$$

where $\varepsilon(\mathbf{k})$ and $\mathbf{\Omega}(\mathbf{k})$ are the conduction band and its Berry curvature, respectively. HHG spectra are evaluated by the Fourier transform of $\mathbf{J}(\tau)$, which is given by

$$\mathbf{J}(\tau) \sim \int \dot{\mathbf{r}}(\tau)\rho(\mathbf{k})d^2\mathbf{k}. \qquad (4)$$

The electron density selectively excited depending on the pulse helicity would be simply approximated by the Dirac delta function, i.e., $\rho(\mathbf{k}) \sim \delta(\mathbf{k} \pm \mathbf{K} + \delta\mathbf{k}_x)$, where the upper (lower) sign indicates a case of the RCP (LCP) pulse and $\delta\mathbf{k}_x$ a possible shift of the electron pocket due to the external bias field along the $\hat{\mathbf{x}}$ direction. The HHG spectrum $I(\omega)$ is obtained, i.e., $I(\omega) \sim \omega^2|\mathbf{J}(\omega)|^2$, and the difference spectrum $D(\omega)$ given by $I_{RCP}(\omega) - I_{LCP}(\omega)$ at $\omega = 3m\omega_0$ is, from Appendix B,

$$D(3m\omega_0) \sim [\Delta\Omega(-\mathbf{K} - \delta\mathbf{k}_x) + \Delta\Omega(\mathbf{K} - \delta\mathbf{k}_x)]$$
$$\times [\Delta\Omega(-\mathbf{K} - \delta\mathbf{k}_x) - \Delta\Omega(\mathbf{K} - \delta\mathbf{k}_x)]$$
$$\sim \langle\Omega\rangle_{net} \times [\Delta\Omega(-\mathbf{K} - \delta\mathbf{k}_x) - \Delta\Omega(\mathbf{K} - \delta\mathbf{k}_x)], \qquad (5)$$

where $\Delta\Omega(\mathbf{k})$ is the Berry curvature change due to the applied strain, i.e., $\Delta\Omega(\mathbf{k}) = \Omega(\mathbf{k}) - \Omega_0(\mathbf{k})$, and $\Omega(\mathbf{k})$ and $\Omega_0(\mathbf{k})$ are the Berry curvatures of the strained monolayer and the pristine monolayer MoS_2, respectively. $D(3m\omega_0)$ is found to

be directly proportional to the net Berry curvature $\langle\Omega\rangle_{net}$ of the conduction band and successfully captures the geometric properties of the electron wave function, and in this sense will be regarded as the dHHG signal. On the other hand, $D(\omega)$ at $\omega = (3m \pm 1)\omega_0$ gives a totally mixed signal, where the dichroic signal cannot be isolated (see Appendix B). Therefore, we hereafter focus on $D(3m\omega_0)$ for the dHHG spectrum.

Unlike Figs. 1(b) and 1(c), we now obtain nonvanishing differences in HHG spectra between RCP and LCP pulses by turning on the bias electric field E_{bias}, i.e., $E_{bias} = 1.0 \times 10^6$ V/m, as shown in Figs. 2(a)–2(d). Under the assumed geometry of Fig. 1(a), the difference spectra at harmonic orders would be considered for each HHG emission along the zigzag direction and the armchair direction of the monolayer MoS_2. In Figs. 2(a) and 2(b), comparisons of HHG spectra along the zigzag direction between RCP and LCP pulses are illustrated at $\epsilon_y = 0$ and $\epsilon_y = 0.3\%$ and in Figs. 2(c) and 2(d); similarly, those along the armchair direction between the RCP and LCP pulses are provided at $\epsilon_y = 0$ and $\epsilon_y = 0.3\%$. It is found that the dHHG signals of $D(3m\omega_0)$ are substantial, especially at the third harmonic order, i.e., $m = 1$.

Employing the first-principles density functional theory [24], one can calculate the Berry curvature of the conduction band of the electron-doped monolayer MoS_2 in Fig. 3(a). The Berry curvature is expressed as

$$\mathbf{\Omega}_n(\mathbf{k}) = \Omega_n(\mathbf{k})\hat{\mathbf{z}} = -\sum_{n'\neq n} 2\,\text{Im}\frac{\langle n\mathbf{k}|\hat{\mathbf{p}}_x|n'\mathbf{k}\rangle\langle n'\mathbf{k}|\hat{\mathbf{p}}_y|n\mathbf{k}\rangle}{[E_{n'}(\mathbf{k}) - E_n(\mathbf{k})]^2}\hat{\mathbf{z}}.$$
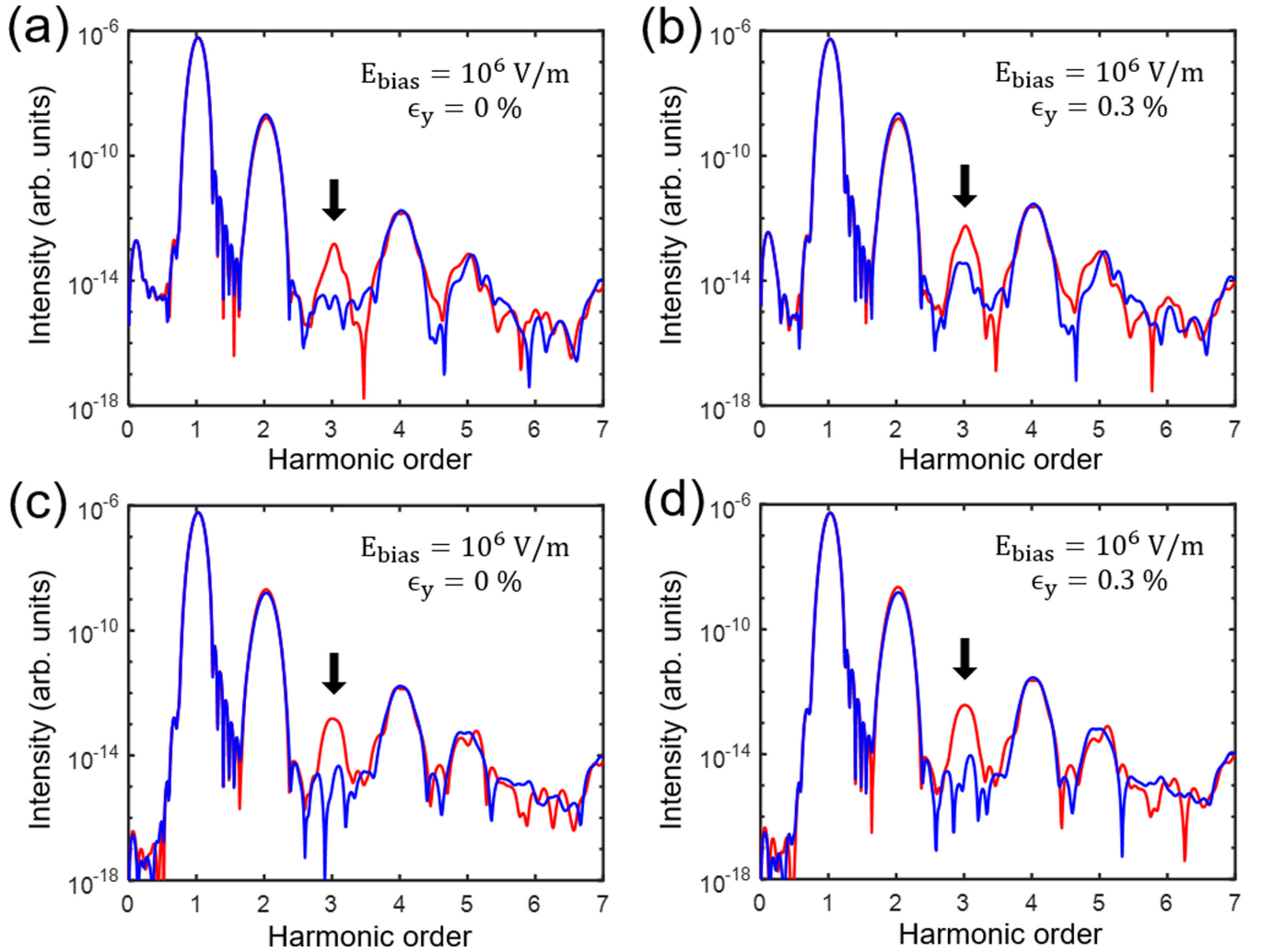$$(6)$$

FIG. 2. HHG spectra under RCP and LCP pulse pumpings. (a,b) HHG spectra along the zigzag direction for RCP (red line) and LCP (blue line) pumpings (a) at $\epsilon_y = 0\%$ and (b) at $\epsilon_y = 0.3\%$ for a fixed bias field $E_{bias} = 10^6$ V/m. (c,d) HHG spectra along the armchair direction for RCP (red line) and LCP (blue line) pulses (c) at $\epsilon_y = 0\%$ and (d) at $\epsilon_y = 0.3\%$. Black arrows indicate the energy position of the third harmonics.

$E_n(\mathbf{k})$ denotes the energy eigenvalue (band energy) of the Bloch state $|n\mathbf{k}\rangle$ (n: band index) and $\hat{\mathbf{p}}_\mu$ the momentum operator along the $\hat{\mu}$ direction. One could then obtain the net Berry curvature $\langle \mathbf{\Omega} \rangle_{net}$ of the conduction band of the doped MoS$_2$ by multiplying the electron density $\rho(\mathbf{k})$ and the Berry curvature of the conduction band $\mathbf{\Omega}(\mathbf{k})$, i.e., $\langle \mathbf{\Omega} \rangle_{net} = \sum_\mathbf{k} \rho(\mathbf{k})\mathbf{\Omega}(\mathbf{k})$. The solid (dashed) line circle in Fig. 3(a) means an area of the electron pocket whose radius is $\sqrt{2\pi n_e/s}$ before (after) applying the bias field with $E_{bias} = 1.0 \times 10^6$ V/m, where the n_e is 0.05 electron per unit cell and s is the unit cell area. A shift of the electron pocket due to the bias field is given by $\delta \mathbf{k} = E_{bias}\tau_{rel}$, where the carrier relaxation time τ_{rel} is 0.5 ps [25]. Based on the generalized gradient approximation (GGA), we consider the electron pockets at the $\mathbf{K}$ or $-\mathbf{K}$ valley by assuming a suitable doping and its asymmetric shift due to the bias field [inset of Fig. 3(a)] and, further, a change of the Berry curvature due to the external uniaxial strain ϵ_y, which enables us to achieve the nonzero net Berry curvature $\langle \mathbf{\Omega} \rangle_{net}$ from the momentum summation over the first Brillouin zone. We take into account the spin-orbit coupling in 201 × 201

k-point grids. In Fig. 3(b), the net Berry curvature of the conduction band, which is much larger than that of the valence band, is delivered with respect to the external strain and the bias field. This should be compared with dHHG signals of $D(3\omega_0)$ of Figs. 3(c) and 3(d) for the HHG emission along the zigzag and armchair directions, respectively. It is confirmed that, as predicted from Eq. (5), Figs. 3(c) and 3(d) give two-dimensional profiles almost indistinguishable from the first-principles calculation of Fig. 3(b). Here we emphasize that, unlike the anomalous Hall effect or the magneto-optical Kerr effect based on electronic and magnetic responses of band carriers, the present dHHG spectral intensity can capture the Berry curvature of the unoccupied empty band.

Next, the phase differences in HHG spectra between RCP and LCP pulses are also interesting. The phase difference, which should be due to the difference in the electron kinematical momenta, would come out in the anomalous current and be eventually realized as the difference in the HHG emission timing between RCP and LCP pulses. We obtain the time-dependent harmonic spectra using the Gabor transformation
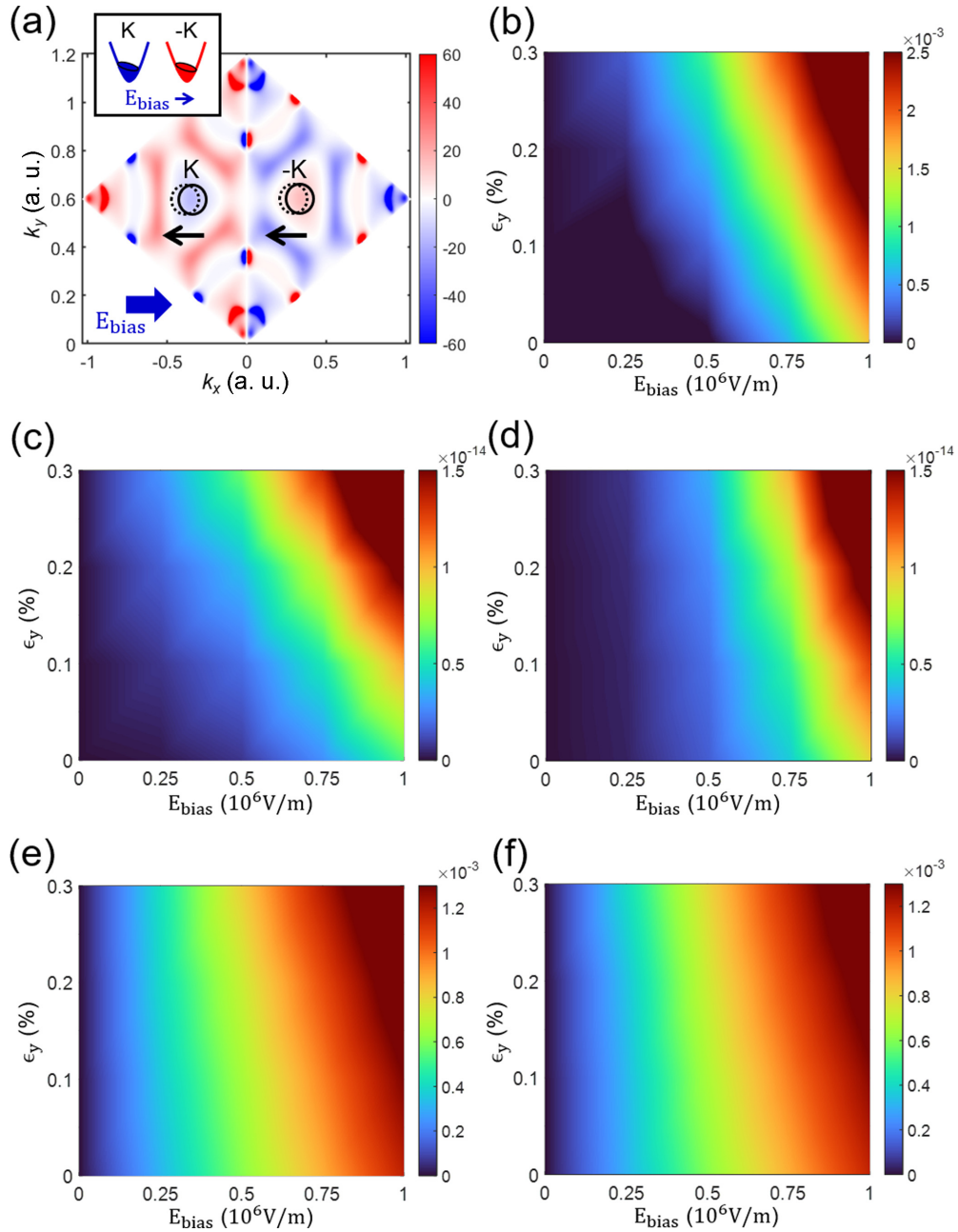
FIG. 3. Net Berry curvature and dHHG signals. (a) First-principles calculation of the Berry curvature of the conduction band of the monolayer MoS_2. Inset shows shifts of the electron pockets by the bias field at a given electron doping. (b) Two-dimensional plot of the first-principles calculation of the net Berry curvature $\langle\Omega\rangle_{net}$ of the conduction band of the monolayer MoS_2 with respect to E_{bias} and ϵ_y. (c,d) Two-dimensional plot of the third-order dHHG spectral intensity $D(3\omega_0)$ with respect to E_{bias} and ϵ_y (c) along the zigzag direction and (d) along the armchair direction. (e,f) Two-dimensional plot of the third-order harmonic emission delay $\Delta\tau_{n=3}$ (e) along the zigzag direction and (f) along the armchair direction.

written as [26,27]

$$G(\omega,\tau) = \int d\tau'\, J(\tau')e^{-\frac{(\tau-\tau')^2}{2\tau_G^2}}\, e^{-i\omega\tau'},$$

where the time window τ_G is 1.2 fs in the calculation. Then we determine the average time $\tau^n_{RCP(LCP)}$ of the nth-order HHG emission under the RCP (LCP) pulse,

$$\tau^n_{RCP(LCP)} = \frac{\int G(n\omega_0,\tau)\tau\, d\tau}{\int G(n\omega_0,\tau)\, d\tau},$$

and evaluate the nth-order harmonic emission delay $\Delta\tau_n$ from $|\tau^n_{RCP}-\tau^n_{LCP}|$. In Figs. 3(e) and 3(f), the delay $\Delta\tau_{n=3}$ from the difference in third-order HHG emission timings between RCP and LCP pulses is provided for each emission along the zigzag direction and the armchair direction. This suggests the time-domain quantification of the nonzero net Berry curvature involved in the dHHG signals.

In Figs. 4(a) and 4(b), the HHG spectra under RCP and LCP pulses adopting pulse energies and field strengths different from those of Fig. 2 or Fig. 3 are provided for a
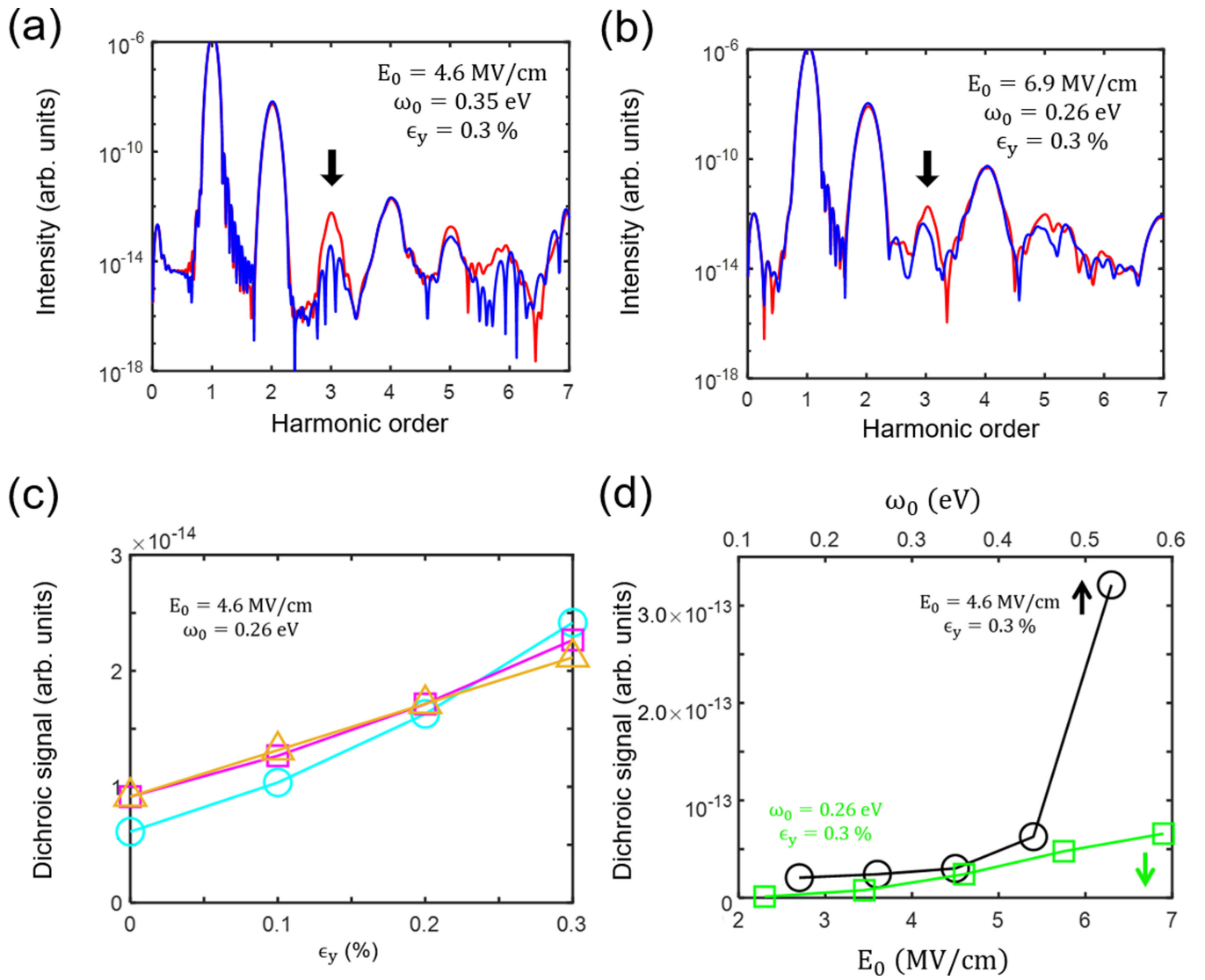
FIG. 4. HHG spectra and dHHG signal strengths at various optical conditions. (a,b) HHG spectra along the zigzag direction for RCP (red line) and LCP (blue line) pulses (a) at $E_0 = 4.6$ MV/cm and $\omega_0 = 0.35$ eV and (b) at $E_0 = 6.9$ MV/cm and $\omega_0 = 0.26$ eV. (c) The third-order dHHG signal intensities along the zigzag (cyan) and armchair (magenta) direction with respect to ϵ_y. Yellow triangles show the net Berry curvature calculated by the first-principles calculation. (d) The third-order dHHG signal intensities along the zigzag direction with respect to ω_0 (black) and E_0 (green). Note that the pulse frequency $\omega_0 \sim 0.5$ eV leading to a rapid increase of the intensity satisfies $3\omega_0 \sim E_{\text{gap}}$.

fixed uniaxial strain $\epsilon_y = 0.3\%$. This readily implies the same behavioral indication of dHHG with respect to the external manipulation parameters as Figs. 3(c)–3(f). In Fig. 4(c), strengths of the dHHG signal are compared between the HHG emission directions and, in Fig. 4(d), those strengths are illustrated with respect to additional optical conditions. Interestingly, the signal strength of Fig. 4(d) is found to abruptly increase around $\omega_0 = 0.5$ eV, which would signify an opening of the interband channel through $3\omega_0 \gtrsim E_{\text{gap}}$. E_{gap} amounts to 1.58 eV in our model. Hence, the conclusion that dHHG could describe developments of the net Berry curvature is confirmed again and found to be robust.

IV. SUMMARY AND CONCLUSION

We investigate HHG and its circular dichroism in undoped monolayer MoS_2 with a quantum master equation. Here we

find that the dichroism of HHG (i.e., dHHG) given by the difference in $3m$th-order HHG spectra between RCP and LCP pulses, especially with $m = 1$, captures the nonzero net Berry curvature of the monolayer MoS_2 when its threefold rotational symmetry is broken by the external strain and the bias electric field. This is found to be essentially the same as the first-principles calculation of the net Berry curvature of the symmetry broken n-doped MoS_2. Finally, we note that hitherto known experimental determinations of the net Berry curvature are for the occupied band on the basis of the electronic and magnetic responses of carriers occupying the band. In contrast, the current finding proposes an experimental challenge to reveal the net Berry curvature of the unoccupied empty band, which suggests a robust insight for the high-intensity field exploration of valleytronic or topological materials.

ACKNOWLEDGMENTS

APPENDIX A: UNIAXIAL STRAIN IN TIGHT-BINDING MODEL

In the monolayer MoS$_2$, Mo d orbitals (d_{z^2}, d_{xy}, and $d_{x^2-y^2}$) are important in constituting the valence and conduction bands. One can make the 3×3 Hamiltonian using these three d orbitals. The matrix elements of the Hamiltonian are then written as

$$H_{ij}(\mathbf{k}) = \sum_{\mathbf{R}} e^{i\mathbf{k}\cdot\mathbf{R}} E_{ij}(\mathbf{R}),$$

$$E_{ij}(\mathbf{R}) = \langle \phi_i(\mathbf{r}) | \hat{H} | \phi_j(\mathbf{r} - \mathbf{R}) \rangle,$$

where $E_{ij}(\mathbf{R})$ and $\phi_i(\mathbf{r})$ are the hopping integral and the atomic orbital. The monolayer MoS$_2$ takes into account Mo-Mo hoppings up to the third nearest neighbors whose distances are $\mathbf{R}_1$, $\mathbf{R}_2$, ..., $\mathbf{R}_1 + \mathbf{R}_2$, ..., $2\mathbf{R}_1$, ..., $2\mathbf{R}_6$ (see Supplemental Material [28]). Now the Hamiltonian is

$$H^{\mathrm{TB}}(\mathbf{k}) = \begin{pmatrix} V_{11} & V_{12} & V_{13} \\ V_{12}^* & V_{22} & V_{23} \\ V_{13}^* & V_{23}^* & V_{33} \end{pmatrix}.$$

For example, V_{11} can be written as

$$V_{11} = \epsilon_1 + 2t_{11}(2\cos\alpha\cos\beta + \cos 2\alpha)$$
$$+ 2r_{11}(2\cos 3\alpha\cos\beta + \cos 2\beta)$$
$$+ 2u_{11}(2\cos 2\alpha\cos 2\beta + \cos 4\alpha),$$

where the parameters are defined as $\alpha = \frac{1}{2}k_x a$, $\beta = \frac{\sqrt{3}}{2}k_y a$, $t_{11} = E_{11}(\mathbf{R}_1)$, $r_{11} = E_{11}(\tilde{\mathbf{R}}_1)$, and $u_{11} = E_{11}(2\mathbf{R}_1)$. ϵ_1 is the on-site energy of the atomic orbital $|\phi_1\rangle$, a the lattice constant, and $\tilde{\mathbf{R}}_1 = \mathbf{R}_1 + \mathbf{R}_2$. More details of the matrix elements are given in Ref. [22]. In the strained monolayer MoS$_2$, the distances are changed according to the applied strain and the related hopping parameters are also changed. Necessary modifications in the matrix elements are obtained by introducing the strain parameter p, i.e., $\beta \to p\beta$ for the uniaxial strain along the $\hat{\mathbf{y}}$ direction (i.e., ϵ_y) and the adjusting parameter s for the hopping parameters associating the strain direction, i.e., $t_{11} \to st_{11}$, $r_{11} \to sr_{11}$, and $u_{11} \to su_{11}$ for the hoppings directly incorporating the uniaxial strain in the lowest-order approximation (see Supplemental Material [28]). We confirm such a parametrization with p and s by comparing the band structure of the model calculation with that of the first-principles calculation. For instance, we can fit parameters from an observation that an application of the strain of $+0.1\%$ ($p = 1.001$) changes the hopping by -0.25% ($s = 0.9975$).

APPENDIX B: DICHROIC HIGH HARMONIC GENERATION

We can write the harmonic current by inserting Eq. (3) into Eq. (4),

$$\mathbf{J}_{\mathrm{RCP(LCP)}}(\tau) \sim \nabla_{\mathbf{k}}\varepsilon[\mp\mathbf{K} - \delta\mathbf{k}_x + \mathbf{A}_{\mathrm{RCP(LCP)}}(\tau)]$$
$$+ e\mathbf{E}_{\mathrm{RCP(LCP)}}(\tau) \times \mathbf{\Omega}[\mp\mathbf{K} - \delta\mathbf{k}_x$$
$$+ \mathbf{A}_{\mathrm{RCP(LCP)}}(\tau)].$$

$\varepsilon(\mathbf{k})$ and $\mathbf{\Omega}(\mathbf{k})$ are the band structure and the Berry curvature under the applied strain. The electron density selectively excited by the pulse helicity can be approximated by $\rho(\mathbf{k}) \sim \delta(\mathbf{k} \pm \mathbf{K} + \delta\mathbf{k}_x)$. $\delta\mathbf{k}_x$ is a shift of the electron pocket due to the bias electric field. Now we rewrite $\mathbf{J}_{\mathrm{RCP(LCP)}}(\tau)$, by keeping the lowest-order terms,

$$\mathbf{J}_{\mathrm{RCP(LCP)}}(\tau)$$
$$\sim \nabla_{\mathbf{k}}\varepsilon_0[\mp\mathbf{K} + \mathbf{A}_{\mathrm{RCP(LCP)}}(\tau)]$$
$$+ \nabla_{\mathbf{k}}(\Delta\varepsilon[\mp\mathbf{K} - \delta\mathbf{k}_x + \mathbf{A}_{\mathrm{RCP(LCP)}}(\tau)])$$
$$+ e\mathbf{E}_{\mathrm{RCP(LCP)}}(\tau) \times \mathbf{\Omega}_0[\mp\mathbf{K} + \mathbf{A}_{\mathrm{RCP(LCP)}}(\tau)]$$
$$+ e\mathbf{E}_{\mathrm{RCP(LCP)}}(\tau) \times \Delta\mathbf{\Omega}[\mp\mathbf{K} - \delta\mathbf{k}_x + \mathbf{A}_{\mathrm{RCP(LCP)}}(\tau)],$$

where $\varepsilon_0(\mathbf{k})$ and $\mathbf{\Omega}_0(\mathbf{k})$ are the band structure and the Berry curvature of the pristine monolayer MoS$_2$. Instead, $\Delta\varepsilon(\mathbf{k})$ and $\Delta\mathbf{\Omega}(\mathbf{k})$ are given by $\varepsilon(\mathbf{k}) - \varepsilon_0(\mathbf{k})$ and $\mathbf{\Omega}(\mathbf{k}) - \mathbf{\Omega}_0(\mathbf{k})$. In order to obtain $\mathbf{J}_{\mathrm{RCP(LCP)}}(\omega)$, we take the Fourier transformation of each term as

$$\mathbf{f}_{0,\,\mathrm{RCP(LCP)}}(\omega) \equiv \mathcal{F}(\nabla_{\mathbf{k}}\varepsilon_0[\mp\mathbf{K} + \mathbf{A}_{\mathrm{RCP(LCP)}}(\tau)]),$$

$$\Delta\mathbf{f}_{\mathrm{RCP(LCP)}}(\omega) \equiv \mathcal{F}[\nabla_{\mathbf{k}}(\Delta\varepsilon[\mp\mathbf{K} - \delta\mathbf{k}_x + \mathbf{A}_{\mathrm{RCP(LCP)}}(\tau)])],$$

$$\mathbf{g}_{0,\,\mathrm{RCP(LCP)}}(\omega) \equiv \mathcal{F}(e\mathbf{E}_{\mathrm{RCP(LCP)}}(\tau)$$
$$\times \mathbf{\Omega}_0[\mp\mathbf{K} + \mathbf{A}_{\mathrm{RCP(RCP)}}(\tau)]),$$

$$\Delta\mathbf{g}_{\mathrm{RCP(LCP)}}(\omega) \equiv \mathcal{F}(e\mathbf{E}_{\mathrm{RCP(LCP)}}(\tau)$$
$$\times \Delta\mathbf{\Omega}[\mp\mathbf{K} - \delta\mathbf{k}_x + \mathbf{A}_{\mathrm{RCP(LCP)}}(\tau)]).$$

Here $\mathcal{F}[\xi(\tau)]$ denotes the Fourier transformation to the frequency space. It should be noted that the $3m$th-order HHG emissions of the pristine monolayer MoS$_2$ are missing as shown in Fig 1(b) [8,9]; that is, $\mathbf{f}_{0,\,\mathrm{RCP(LCP)}}(\omega) + \mathbf{g}_{0,\,\mathrm{RCP(LCP)}}(\omega)$ vanishes at $\omega = 3m\omega_0$. In the lowest-order approximation [via the Taylor expansion keeping the lowest-order term of $\mathbf{A}_{\mathrm{RCP(LCP)}}(\tau)$], the harmonic generation $I(\omega)$, i.e., $I(\omega) \sim \omega^2 |\mathbf{J}(\omega)|^2$, at $\omega = 3m\omega_0$ along the $\hat{\mathbf{x}}$ (zigzag) and $\hat{\mathbf{y}}$ (armchair) directions is now

$$I_{\mathrm{RCP(LCP)};\,x}(\omega) \sim \omega^2 |\Delta f_{\mathrm{RCP(LCP)};\,x}(\omega) \pm i\Delta g_{\mathrm{RCP(LCP)};\,x}(\omega)|^2,$$

$$I_{\mathrm{RCP(LCP)};\,y}(\omega) \sim \omega^2 |\Delta g_{\mathrm{RCP(LCP)};\,y}(\omega)|^2.$$

Then, the difference spectrum $D_\mu(\omega) = I_{\mathrm{RCP};\,\mu}(\omega) - I_{\mathrm{LCP};\,\mu}(\omega)$ at $\omega = 3m\omega_0$ along the $\hat{\mu}$ direction is

$$D_\mu(\omega) \propto [\Delta g_{\mathrm{RCP};\,\mu}(\omega)]^2 - [\Delta g_{\mathrm{LCP};\,\mu}(\omega)]^2$$
$$= [\Delta g_{\mathrm{RCP};\,\mu}(\omega) + \Delta g_{\mathrm{LCP};\,\mu}(\omega)]$$
$$\times [\Delta g_{\mathrm{RCP};\,\mu}(\omega) - \Delta g_{\mathrm{LCP};\,\mu}(\omega)]$$

for both $\hat{\boldsymbol{\mu}} = \hat{\mathbf{x}}$ [$\Delta f_{\text{RCP}; x}(\omega) \approx \Delta f_{\text{LCP}; x}(\omega)$ should be noted] and $\hat{\boldsymbol{\mu}} = \hat{\mathbf{y}}$. This clearly delivers a message that the $3m$th-order difference spectra $D_\mu(3m\omega_0)$ directly capture the net Berry curvature $\langle\Omega\rangle_{\text{net}}$, i.e., [$\Delta g_{\text{RCP}; \mu}(\omega) + \Delta g_{\text{LCP}; \mu}(\omega)$], and deserve the true dHHG

signal. On the other hand, for the $(3m \pm 1)$-th order HHG emission, $\mathbf{f}_{0, \text{RCP(LCP)}}(\omega) + \mathbf{g}_{0, \text{RCP(LCP)}}(\omega)$ does not vanish so that the difference spectra give a totally mixed signal. One cannot isolate the dichroic signal any further.

[1] D. Xiao, M.-C. Chang, and Q. Niu, Berry phase effects on electronic properties, Rev. Mod. Phys. **82**, 1959 (2010).

[2] K. F. Mak, K. L. McGill, J. Park, and P. L. McEuen, The valley Hall effect in MoS$_2$ transistors, Science **344**, 1489 (2014).

[3] X. Xu, W. Yao, D. Xiao, and T. F. Heinz, Spin and pseudospins in layered transition metal dichalcogenides, Nat. Phys. **10**, 343 (2014).

[4] T. Cao, G. Wang, W. Han, H. Ye, C. Zhu, J. Shi, Q. Niu, P. Tan, E. Wang, B. Liu, and J. Feng, Valley-selective circular dichroism of monolayer molybdenum disulphide, Nat. Commun. **3**, 887 (2014).

[5] J. Lee, Z. Wang, H. Xie, K. F. Mak, and J. Shan, Valley magnetoelectricity in single-layer MoS$_2$, Nat. Mater. **16**, 887 (2017).

[6] Y. Kim and J. D. Lee, Anomalous electron dynamics induced through the valley magnetic domain: A pathway to valleytronic current processing, Nano Lett. **19**, 4166 (2019).

[7] S. Ghimire and D. A. Reis, High-harmonic generation from solids, Nat. Phys. **15**, 10 (2019).

[8] O. E. Alon, V. Averbukh, and N. Moiseyev, Selection Rules for the High Harmonic Generation Spectra, Phys. Rev. Lett. **80**, 3743 (1998).

[9] X. Liu, X. Zhu, L. Li, Y. Li, Q. Zhang, P. Lan, and P. Lu, Selection rules of high-order-harmonic generation: Symmetries of molecules and laser fields, Phys. Rev. A **94**, 033410 (2016).

[10] S. Ghimire, A. D. DiChiara, E. Sistrunk, P. Agostini, L. F. DiMauro, and D. A. Reis, Observation of high-order harmonic generation in a bulk crystal, Nat. Phys. **7**, 138 (2011).

[11] N. Yoshikawa, T. Tamaya, and K. Tanaka, High-harmonic generation in graphene enhanced by elliptically polarized light excitation, Science **356**, 736 (2017).

[12] H. Nishidome, K. Nagai, K. Uchida, Y. Ichinose, Y. Yomogida, Y. Miyata, K. Tanaka, and K. Yanagi, Control of high-harmonic generation by tuning the electronic structure and carrier injection, Nano Lett. **20**, 6215 (2020).

[13] R. E. F. Silva, Á. Jiménez-Galán, B. Amorim, O. Smirnova, and M. Ivanov, Topological strong-field physics on sub-laser-cycle timescale, Nat. Photonics **13**, 849 (2019).

[14] H. Liu, Y. Li, Y. S. You, S. Ghimire, T. F. Heinz, and D. A. Reis, High-harmonic generation from an atomically thin semiconductor, Nat. Phys. **13**, 262 (2017).

[15] T. T. Luu and H. J. Wörner, Measurement of the Berry curvature of solids using high-harmonic spectroscopy, Nat. Commun. **9**, 916 (2018).

[16] C. P. Schmid, L. Weigl, P. Grössing, V. Junk, C. Gorini, S. Schlauderer, S. Ito, M. Meierhofer, N. Hofmann, D. Afanasiev, J. Crewse, K. A. Kokh, O. E. Tereshchenko, J. Güdde, F. Evers, J. Wilhelm, K. Richter, U. Höfer, and R. Huber, Tunable non-integer high-harmonic generation in a topological insulator, Nature (London) **593**, 385 (2021).

[17] G. P. Zhang, M. S. Si, M. Murakami, Y. H. Bai, and T. F. George, Generating high-order optical and spin harmonics from ferromagnetic monolayers, Nat. Commun. **9**, 3031 (2018).

[18] J. L. Krause, K. J. Schafer, and K. C. Kulander, High-Order Harmonic Generation from Atoms and Ions in the High Intensity Regime, Phys. Rev. Lett. **68**, 3535 (1992).

[19] T. Zuo, A. D. Bandrauk, M. Ivanov, and P. B. Corkum, Control of high-order harmonic generation in strong laser fields, Phys. Rev. A **51**, 3991 (1995).

[20] N. Yoshikawa, K. Nagai, K. Uchida, Y. Takaguchi, S. Sasaki, Y. Miyata, and K. Tanaka, Interband resonant high-harmonic generation by valley polarized electron-hole pairs, Nat. Commun. **10**, 3709 (2019).

[21] S. A. Sato, H. Hirori, Y. Sanari, Y. Kanemitsu, and A. Rubio, High-order harmonic generation in graphene: Nonlinear coupling of intraband and interband transitions, Phys. Rev. B **103**, L041408 (2021).

[22] G.-B. Liu, W.-Y. Shan, Y. Yao, W. Yao, and D. Xiao, Three-band tight-binding model for monolayers of group-VIB transition metal dichalcogenides, Phys. Rev. B **88**, 085433 (2013).

[23] P. Johari and V. B. Shenoy, Tuning the electronic properties of semiconducting transition metal dichalcogenides by applying mechanical strains, ACS Nano **6**, 5449 (2012).

[24] See http://elk.sourceforge.net.

[25] Z. Jin, X. Li, J. T. Mullen, and K. W. Kim, Intrinsic transport properties of electrons and holes in monolayer transition-metal dichalcogenides, Phys. Rev. B **90**, 045422 (2014).

[26] I. Floss, C. Lemell, G. Wachter, V. Smejkal, S. A. Sato, X.-M. Tong, K. Yabana, and J. Burgdörfer, *Ab initio* multiscale simulation of high-order harmonic generation in solids, Phys. Rev. A **97**, 011401(R) (2018).

[27] C. Yu, H. Iravani, and L. B. Madsen, Crystal-momentum-resolved contributions to multiple plateaus of high-order harmonic generation from band-gap materials, Phys. Rev. A **102**, 033105 (2020).

[28] See Supplemental Material at http://link.aps.org/supplemental/10.1103/PhysRevB.106.205422 for details of tight-binding model and calculation.